Nonuniqueness of local stress of three-body potentials in molecular simulations

Koh M. Nakagawa and Hiroshi Noguchi[*]

Institute for Solid State Physics, University of Tokyo, Kashiwa, Chiba 277-8581, Japan

Microscopic stress fields are widely used in molecular simulations to understand mechanical behavior. Recently, decomposition methods of multibody forces to central force pairs between the interacting particles have been proposed. Here, we introduce a force center of a three-body potential and propose different force decompositions that also satisfy the conservation of translational and angular momentum. We compare the force decompositions by stress-distribution magnitude and discuss their difference in the stress profile of a bilayer membrane by using coarse-grained and atomistic molecular dynamics simulations.

I. INTRODUCTION

The stress tensor is a fundamental quantity that connects discrete molecular systems and continuum mechanics. The calculation of the local stress field from molecular simulations has a long history [1–14]. Irving and Kirkwood introduced the microscopic stress tensor formula based on nonequilibrium statistical mechanics [1], following which a rigorous mathematical formula was proposed by Noll [2]. In the following, we refer to their procedure as the Irving–Kirkwood–Noll (IKN) procedure, as stated by Admal and Tadmor [8]. Hardy introduced the spatial averaging of the stress tensor using weighting functions to improve statistics [3]. However, these procedures are limited to systems in which interactions consist of pairwise forces.

The method to map the stress of multibody potentials into the continuum space has been debated. Multibody potentials have been frequently used in molecular simulations. Bending and dihedral potentials, which are widely used, are three- and four-body potentials, respectively. The interaction between adjacent dihedrals is represented by five-body correction map (CMAP) potential in the Chemistry at Harvard Macromolecular Mechanics (CHARMM) force field [13,15]. A curvature potential in meshless membranes is a function of three rotational invariants of the weighted gyration tensor and produces n-body forces, where n depends on the local density [16]. Since most of the multibody forces are not central forces between particles, the IKN procedure cannot be directly applied to them. Note that multibody hydrophobic potentials as a function of the local hydrophobic particle density for proteins [17] and membranes [16,18] give central forces between particles so that their stress can be calculated directly by using the IKN procedure.

Goetz and Lipowsky proposed a decomposition procedure for multibody potentials [6] based on Schofield and Henderson's procedure [4]. Multibody forces are decomposed into pairwise (noncentral) forces, and the IKN procedure is applied to each decomposed force pair. We refer to this method as Goetz–Lipowsky decomposition (GLD). However, GLD does not satisfy the strong law of action and reaction, as pointed out by Admal and Tadmor [8,9], while it satisfies the weak law of action and reaction: GLD conserves translational momentum

but not angular momentum. Consequently, the stress tensor is not symmetric. To overcome this problem, central force decomposition (CFD) was proposed [8,9,11–13]. The forces decomposed using CFD satisfy the strong law of action and reaction so that the stress tensor is symmetric by construction. The original CFD is limited to three- or four-body forces because there exists a unique force decomposition for only up to four-body forces. For n-body forces with $n \geqslant 5$, the number of degrees of freedom, $3n - 6$, is less than the number of pairs, $n(n - 1)/2$, in the three-dimensional (3D) space. Very recently, the generalization to more than four-body forces, which is called a covariant CFD (cCFD), was introduced by Torres-Sánchez *et al.* [13,14]. The application to a structural coiled-coil protein with the five-body CMAP potential was demonstrated [13].

In this paper, we discuss nonuniqueness in the force decomposition of three-body forces in classical mechanics. Three-body forces can be uniquely decomposed by CFD. However, we will show different decompositions, which also satisfy the strong law of action and reaction. A force center can be uniquely defined for three-body forces, and the forces are decomposed into central force pairs between interacting particles and the force center. To combine this decomposition and CFD, the position of the force center can be arbitrarily taken. This nonuniqueness is related with the nonunique potential-energy extension discussed in Refs. [8–10]. It is a specific case of the degeneracy of four-body forces into two-dimensional (2D) space. We will discuss the choice of this center position by the stress distribution. Although two-body forces can also similarly be decomposed, the IKN procedure always gives the minimum stress distribution. In contrast, the stress distribution of three-body forces depends on the type of the forces. We will also discuss the influence of the resolution of simulation models.

For an application of the force decomposition, we investigated a bilayer membrane by using coarse-grained and atomistic molecular dynamics (MD) simulations. The stress profile along the normal direction has been widely calculated in the molecular simulations of lipid membranes. Two opposing forces, interfacial tension and steric repulsion, produce the inhomogeneous stress inside the bilayers [19]. This inhomogeneity is a key property of the bilayers because it determines the area per lipid molecule [19], spontaneous curvature [20–24], Gaussian curvature modulus [21–28], and function of the mechanosensitive channel [29,30]. Since the stress profile

---
[*]noguchi@issp.u-tokyo.ac.jp

cannot be obtained experimentally [31,32], estimation by using molecular simulations is important. Recently, however, Torres–Sánchez *et al.* reported that the stress profile is strongly dependent on the force decomposition method [13]. The dihedral forces give the largest contribution to the stress profile by CFD. We show that the stress profile is largely dependent on the decomposition of bending forces.

In Sec. II, we discuss the force decomposition method. After introducing the existing decomposition method, we describe the alternative decomposition method for three-body forces. As an example, we show the decomposition for an area potential and a bending potential. The area potential is one of the simplest three-body potentials and is connected to continuum mechanics in a straightforward manner. The bending potential is the most widely used three-body potential. In Sec. III, the bilayer membrane is examined. The stress profile and Gaussian curvature modulus are calculated for different decomposition methods. The discussion and summary are given in Secs. IV and V, respectively.

II. FORCE DECOMPOSITION

A. Irving–Kirkwood–Noll procedure

Stress averaged over the entire simulation box is given by the virial as

$$\boldsymbol{\sigma} = \boldsymbol{\sigma}_{\text{K}} + \boldsymbol{\sigma}_{\text{U}}, \tag{1}$$

$$\boldsymbol{\sigma}_{\text{K}} = -\frac{1}{V} \sum_i \langle m_i \mathbf{v}_i \otimes \mathbf{v}_i \rangle, \tag{2}$$

$$\boldsymbol{\sigma}_{\text{U}} = -\frac{1}{V} \sum_i \langle \mathbf{f}_i \otimes \mathbf{r}_i \rangle, \tag{3}$$

$$= \frac{1}{V} \sum_{n=2}^{N} \sum_{k_n=1}^{n} \sum_{i=1}^{n} \left\langle \frac{\partial U_{k_n}}{\partial \mathbf{r}_{k_n,i}} \otimes \left(\mathbf{r}_i - \mathbf{r}_{k_n,0} \right) \right\rangle, \tag{4}$$

where m_i, $\mathbf{r}_i$, and $\mathbf{v}_i$ are the mass, position, and velocity of the ith particle and $\mathbf{f}_i = -\partial U / \partial \mathbf{r}_i$. The symbol $\otimes$ denotes a tensor product and $\langle \ldots \rangle$ denotes a statistical average. This global stress is uniquely determined even for multibody forces. The potential contribution $\boldsymbol{\sigma}_{\text{U}}$ can be rewritten with Eq. (4) by using cluster expansion [14] as

$$U(\mathbf{r}_1, \ldots, \mathbf{r}_N) = \sum_{n=2}^{N} \sum_{k_n=1} U_{k_n} \left(\mathbf{r}_{k_n,1}, \ldots, \mathbf{r}_{k_n,n} \right), \tag{5}$$

where each U_{k_n} is an n-body potential that is invariant under translation and rotation. The origin $\mathbf{r}_{k_n,0}$ of the positions can be taken differently for each U_{k_n}, as expressed in Eq. (4). Each origin can be arbitrarily chosen but a position close to interacting particles is preferred to reduce numerical errors, particularly for large-scale simulations. When the origin is set to the position of one of the interacting particles, the potential stress of the pairwise potentials takes the well-known form

$$\boldsymbol{\sigma}_{\text{U,pair}} = -\frac{1}{V} \sum_{i<j} \langle f_{ij} \hat{\mathbf{r}}_{ij} \otimes \mathbf{r}_{ij} \rangle, \tag{6}$$

where $f_{ij} = -\partial U_{k_2} / \partial r_{ij}$, $\mathbf{r}_{ij} = \mathbf{r}_i - \mathbf{r}_j$, $r_{ij} = |\mathbf{r}_{ij}|$, and $\hat{\mathbf{r}}_{ij} = \mathbf{r}_{ij}/r_{ij}$. Under a periodic boundary condition, the periodic image is used instead of the original position when the potential interaction crosses the periodic boundary.

For pairwise interactions, the local stress at a position $\mathbf{x}$ is given by the IKN procedure as [1,2]

$$\boldsymbol{\sigma}(\mathbf{x}) = \boldsymbol{\sigma}_{\text{K}}(\mathbf{x}) + \boldsymbol{\sigma}_{\text{U}}(\mathbf{x}), \tag{7}$$

$$\boldsymbol{\sigma}_{\text{K}}(\mathbf{x}) = -\sum_i \langle m_i \mathbf{v}_i \otimes \mathbf{v}_i \delta(\mathbf{r}_i - \mathbf{x}) \rangle, \tag{8}$$

$$\boldsymbol{\sigma}_{\text{U}}(\mathbf{x}) = -\sum_{i<j} \langle f_{ij} \hat{\mathbf{r}}_{ij} \otimes \mathbf{r}_{ij} B(\mathbf{r}_i, \mathbf{r}_j, \mathbf{x}) \rangle, \tag{9}$$

where $B(\mathbf{r}_i, \mathbf{r}_j, \mathbf{x}) = \int_0^1 \delta[(1-s)\mathbf{r}_i + s\mathbf{r}_j - \mathbf{x}]ds$. The force propagates along the line segment between $\mathbf{r}_i$ and $\mathbf{r}_j$. This local stress tensor is symmetric: $\sigma_{\alpha\beta}(\mathbf{x}) = \sigma_{\beta\alpha}(\mathbf{x})$ for $\alpha, \beta \in \{x, y, z\}$.

B. Central force and geometric-center decompositions

When the multibody force is decomposed into pairwise forces between interacting particles, the IKN procedure for pairwise forces is applicable. Therefore, decomposition methods to pairwise forces have been focused upon. Goetz and Lipowsky proposed a decomposition (GLD) $\mathbf{f}_{ij} = (\mathbf{f}_i - \mathbf{f}_j)/n$ for n-body forces [6]. This decomposition conserves translational momentum but does not conserve angular momentum, since the force $\mathbf{f}_{ij}$ is not generally parallel to $\mathbf{r}_{ij}$.

To satisfy the conservation of the angular momentum as well, Admal and Tadmor proposed the decomposition to central forces between interacting particles (CFD) [8,9]. Three-body forces can be uniquely decomposed by CFD:

$$\begin{aligned} \mathbf{f}_1 &= f_{12}\hat{\mathbf{r}}_{12} + f_{13}\hat{\mathbf{r}}_{13}, \\ \mathbf{f}_2 &= f_{23}\hat{\mathbf{r}}_{23} + f_{12}\hat{\mathbf{r}}_{21}, \\ \mathbf{f}_3 &= f_{13}\hat{\mathbf{r}}_{31} + f_{23}\hat{\mathbf{r}}_{32}. \end{aligned} \tag{10}$$

Since the translational and angular momenta are conserved, $\mathbf{f}_1 + \mathbf{f}_2 + \mathbf{f}_3 = \mathbf{0}$ and $\mathbf{f}_1 \times \mathbf{r}_1 + \mathbf{f}_2 \times \mathbf{r}_2 + \mathbf{f}_3 \times \mathbf{r}_3 = \mathbf{0}$. For $f_{12} > 0$, f_{12} is a repulsive force between $\mathbf{r}_1$ and $\mathbf{r}_2$. From Eq. (10), f_{12} is given by

$$f_{12} = \frac{\mathbf{f}_1 \cdot \hat{\mathbf{r}}_{12} - (\mathbf{f}_1 \cdot \hat{\mathbf{r}}_{13})(\hat{\mathbf{r}}_{12} \cdot \hat{\mathbf{r}}_{13})}{1 - (\hat{\mathbf{r}}_{12} \cdot \hat{\mathbf{r}}_{13})^2}, \tag{11}$$

or

$$f_{12} = \frac{1}{2} \left(\frac{\mathbf{f}_1 \cdot (\hat{\mathbf{r}}_{12} + \hat{\mathbf{r}}_{13})}{1 + \hat{\mathbf{r}}_{12} \cdot \hat{\mathbf{r}}_{13}} + \frac{\mathbf{f}_2 \cdot (\hat{\mathbf{r}}_{23} + \hat{\mathbf{r}}_{21})}{1 + \hat{\mathbf{r}}_{21} \cdot \hat{\mathbf{r}}_{23}} - \frac{\mathbf{f}_3 \cdot (\hat{\mathbf{r}}_{31} + \hat{\mathbf{r}}_{32})}{1 + \hat{\mathbf{r}}_{31} \cdot \hat{\mathbf{r}}_{32}} \right). \tag{12}$$

Similarly, f_{13} and f_{23} are given. Equation (12) is recommended for numerical calculations, since it gives smaller numerical errors when two angles of $\triangle 123$ are close to null and the third is close to π. Alternatively, these force pairs can be derived directly from $f_{12} = -\partial U_{k_3} / \partial r_{12}|_{r_{13}, r_{23}}$ [8], as demonstrated for the area and bending potentials in Appendixes A and B, respectively. The CFDs of the area expansion and bending forces are shown in Figs. 1(b) and 2(b), respectively. The three interacting particles form a triangle and lie on a plane so that the forces $\mathbf{f}_1$, $\mathbf{f}_2$, and $\mathbf{f}_3$ are along this plane owing to the conservation of translational and angular momenta. Hence, we can consider the 2D space without loss of generality.
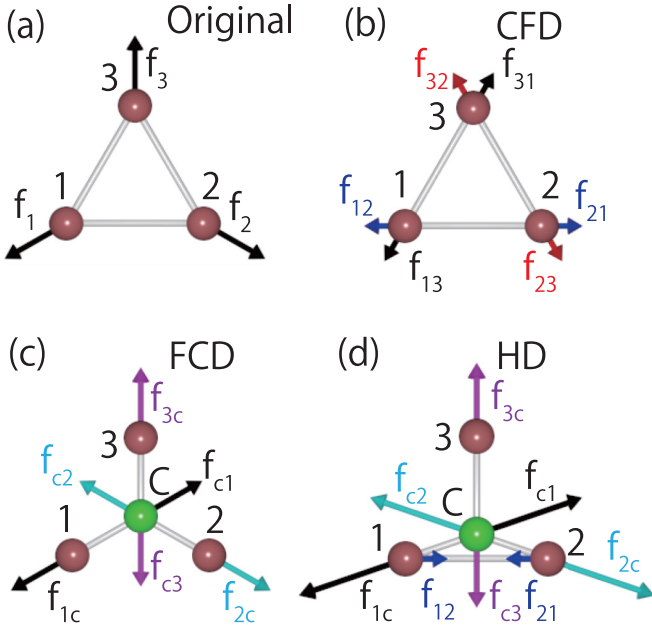
FIG. 1. Force decomposition for area expansion forces: (a) original forces, (b) CFD, (c) FCD, (d) HD. The light gray (green) sphere represents the force center, $\mathbf{r}_c$.

Alternatively, Heinz *et al.* proposed a decomposition method that uses the geometric center, $\sum_i^{n'} \mathbf{r}_i/n'$, of n' interacting particles in a divided cell for an n-body potential ($n' < n$) [7]. In this decomposition, the angular momentum is not conserved. The geometric center is determined only by the positions and has no relation to the force balance. Hence, the geometric center can significantly deviate from the positions where the forces act. For example, when great forces act only
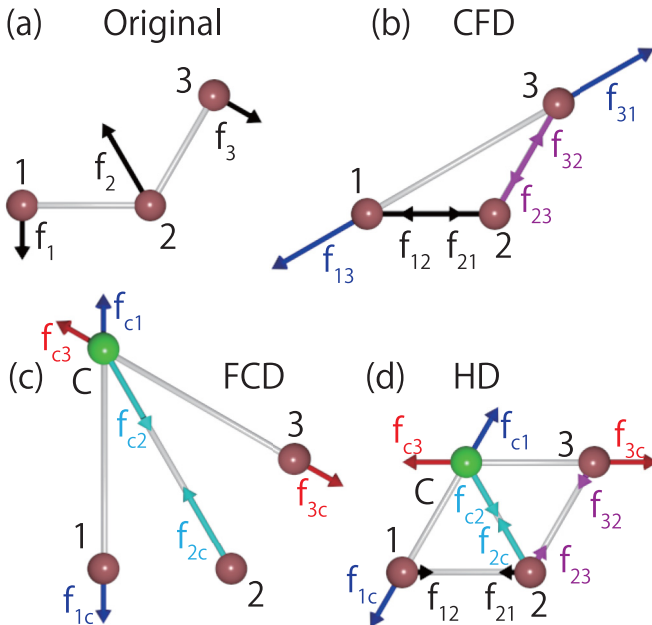

FIG. 2. Force decomposition for bending forces on θ_{123}: (a) original forces, (b) CFD, (c) FCD, (d) HD. The same color notation as Fig. 1 is employed.

on two particles in n-body forces, i.e., $|\mathbf{f}_i| \gg |\mathbf{f}_j|$ ($i = 1, 2$, and $j \geqslant 3$), the resultant stress should be close to that of the pairwise forces between $\mathbf{r}_1$ and $\mathbf{r}_2$. However, the geometric center can be far from the line segment between $\mathbf{r}_1$ and $\mathbf{r}_2$. Thus, a center position should be determined by the force balance, or a specific force decomposition should be employed for a chosen center position to satisfy the force balance. We consider the center position with the decomposition to satisfy the strong law of the action and reaction in Sec. II C.

One may consider the center of mass as an alternative candidate for the center position. However, the potential stress term $\boldsymbol{\sigma}_U$ is not dependent on mass distribution in thermal equilibrium. One can calculate $\boldsymbol{\sigma}_U$ by using a Monte Carlo simulation, in which the mass distribution is not required at all. Since the values of the particle masses are arbitrary but positive, the center of mass lies inside the convex polyhedron (triangle for three-body forces) formed by interacting particles. As described below, it is important whether the center position for force decomposition is inside or outside the triangle for three-body forces.

C. Force center and hybrid decompositions

We consider the alternative decompositions of three-body forces. As mentioned above, the forces are uniquely determined by CFD for three-body forces. However, when one more position is taken into account, the forces are not uniquely determined. For three-body forces, three lines drawn along the force vectors $\mathbf{f}_i$ from the particle positions $\mathbf{r}_i$ ($i \in 1,2,3$) always meet at one position owing to the angular-momentum conservation. We refer to this position as the force center, $\mathbf{r}_c$. It is determined as

$$\mathbf{r}_c = \frac{1}{q}(\tilde{f}_{12}\tilde{f}_{13}\mathbf{r}_1 + \tilde{f}_{12}\tilde{f}_{23}\mathbf{r}_2 + \tilde{f}_{13}\tilde{f}_{23}\mathbf{r}_3), \qquad (13)$$

$$q = \tilde{f}_{12}\tilde{f}_{13} + \tilde{f}_{12}\tilde{f}_{23} + \tilde{f}_{13}\tilde{f}_{23}, \qquad (14)$$

where $\tilde{f}_{ij} = f_{ij}/r_{ij}$ and f_{ij} are the forces obtained by CFD. The sign of the denominator q determines the region of the force center as described later. By using the force center, the forces are decomposed into three central force pairs $f_{ic}\hat{\mathbf{r}}_{ic} = \mathbf{f}_i$ between $\mathbf{r}_i$ and $\mathbf{r}_c$ for $i \in \{1,2,3\}$ [see Figs. 1(c) and 2(c)]. We refer to this decomposition as force-center decomposition (FCD). Since these are central forces, the strong law of action and reaction is satisfied and the symmetric local stress tensor is obtained by the IKN procedure for these decomposed forces.

When three force pairs have the same sign ($f_{12} > 0$, $f_{13} > 0$, $f_{23} > 0$ or $f_{12} < 0$, $f_{13} < 0$, $f_{23} < 0$), the force center lies in the interior region of the triangle $\triangle 123$ and $q > 0$. For an expansion force as shown in Fig. 1, the decomposed forces in CFD and FCD can be physically interpreted as line (surface) tension on the edge of the triangular region and pressure of the interior region on the particles, respectively.

The exterior region can be divided into six regions, as shown in Fig. 3. When $f_{12}f_{13} > 0$ and $f_{12}f_{23} < 0$, the force center lies in the region A or D for $q > 0$ or $q < 0$, respectively. For bending potentials as a function of the angle $\theta_{123} = \cos^{-1}(\hat{\mathbf{r}}_{12} \cdot \hat{\mathbf{r}}_{32})$, $\mathbf{r}_c$ always lies outside the triangle and $q < 0$. As θ_{123} becomes closer to π, $\mathbf{f}_1$ and $\mathbf{f}_3$ approach parallel lines so that $\mathbf{r}_c$ becomes further from the particle positions. The
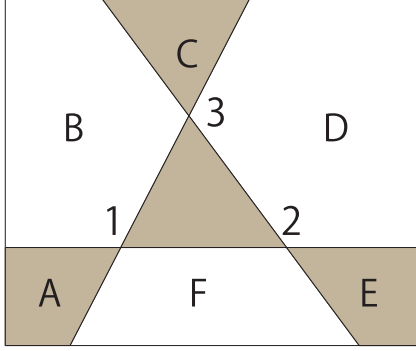
FIG. 3. Six exterior regions (A–F) of the triangle $\triangle 123$. Shaded and white regions correspond to $q > 0$ and $q < 0$, respectively.

details of decomposition for the area and bending potentials are described in Appendixes A and B, respectively.

The force-center position can be moved by combining FCD with CFD. We refer to this combined decomposition as hybrid decomposition (HD). If necessary to distinguish them, the force center in FCD is called the original force center $\mathbf{r}_{c0}$. In HD, the force pair of each edge of $\triangle 123$ is divided into FCD and CFD components as $f_{12}^{\text{all}} = f_{12}^{\text{FC}} + f_{12}^{\text{CF}}$. The force center $\mathbf{r}_c$ is determined by Eq. (13) with the FCD components f_{12}^{FC}, f_{13}^{FC}, and f_{23}^{FC}. For example, Fig. 1(d) shows the decomposition into three force pairs with $\mathbf{r}_c$ and one force pair along $\mathbf{r}_{12}$. When the contribution of force f_{12} to FCD increases (decreases), the hybrid force center $\mathbf{r}_c$ is further (closer) to $\mathbf{r}_3$ than the original force center $\mathbf{r}_{c0}$ [see Eq. (13)]. Figure 2(d) shows HD combining FCD with two force pairs along $\mathbf{r}_{12}$ and $\mathbf{r}_{23}$. If the force center lies on the edge of the triangle $\triangle 123$, the resultant decomposition coincides with CFD (if $\mathbf{r}_c$ lies in the middle of the line segment between $\mathbf{r}_2$ and $\mathbf{r}_3$, then $f_{1c} = 0$).

The hybrid decomposition can be applied to two-body forces if two symmetric positions, $\mathbf{r}_3$ and $\mathbf{r}_4$, are employed as shown in Fig. 4, where $r_{14} = r_{13} = r_{24} = r_{23}$. Therefore, the IKN procedure is not a unique solution to obtain the stress tensor even for the two-body forces. However, the total length ($\ell_{\text{sum}} = \sum_{i<j} r_{ij}$) and force norm sum ($f_{\text{sum}} = \sum_{i<j} |f_{ij}|$)

FIG. 4. Force decomposition for two-body forces: (a) original forces, (b) example of the hybrid decompositions, (c) stress distribution magnitude Γ of two-body forces as a function of θ. It is normalized by the magnitude Γ_0 obtained by the IKN procedure.

become greater than the IKN procedure. Thus, the IKN procedure is the best decomposition method for two-body forces.

D. Stress distribution

Although the force center can be set to an arbitrary position in HD, positions that are excessively far away are not physically suitable. Thus, we need a criterion to select the decomposition. We consider the minimization of the stress distribution as a candidate criterion. Hence, we define the stress-distribution magnitude Γ as a summation over the cross norm of the stress,

$$\Gamma = \sum_{i<j} |f_{ij}| r_{ij}, \qquad (15)$$

where the summation is taken over all pairs ($i,j \in 1,2,3,c$ for the three-body forces).

For the two-body forces, the IKN procedure always gives the minimum value of Γ. Therefore, Γ can be employed as the criterion for the two-body forces. For the decomposition shown in Fig. 4(b), the magnitude is given as $\Gamma = |f_{12}| r_{12}(1 + 2 \tan^2 \theta)$ and has the minimum at $\theta = 0$ [see Fig. 4(c)].

In the following, we consider the minimization problem of Γ for three-body forces. For CFD and FCD, $\Gamma_{\text{CFD}} = |f_{12}| r_{12} + |f_{13}| r_{13} + |f_{23}| r_{23}$ and $\Gamma_{\text{FCD}} = |f_{1c}| r_{1c} + |f_{2c}| r_{2c} + |f_{3c}| r_{3c}$, respectively. Interestingly, when the original force center exists in the interior region of the triangle $\triangle 123$, these two magnitudes take the same value: $\Gamma_{\text{CFD}} = \Gamma_{\text{FCD}}$. The force norm sum f_{sum} of CFD is less than that of FCD, while the total length ℓ_{sum} of CFD is greater. For HD with $\mathbf{r}_c$ lying in the interior region of $\triangle 123$,

$$\Gamma_{\text{HD}} = \Gamma_{\text{HD}}^{\text{FC}} + \Gamma_{\text{HD}}^{\text{CF}} \qquad (16)$$
$$= (|f_{12}^{\text{FC}}| + |f_{12}^{\text{CF}}|) r_{12} + (|f_{13}^{\text{FC}}| + |f_{13}^{\text{CF}}|) r_{13}$$
$$+ (|f_{23}^{\text{FC}}| + |f_{23}^{\text{CF}}|) r_{23}. \qquad (17)$$

When the CFD and FCD components in each force pair have the same sign, i.e., when $f_{12}^{\text{CF}} f_{12}^{\text{FC}} > 0$, $|f_{12}^{\text{all}}| = |f_{12}^{\text{CF}}| + |f_{12}^{\text{FC}}|$ so that $\Gamma_{\text{HD}} = \Gamma_{\text{CFD}}$. When $f_{12}^{\text{CF}} f_{12}^{\text{FC}} < 0$, $|f_{12}^{\text{all}}| < |f_{12}^{\text{CF}}| + |f_{12}^{\text{FC}}|$ so that $\Gamma_{\text{HD}} > \Gamma_{\text{CFD}}$. For the hybrid force center inside the triangle $\triangle 123$, the decomposition with the same sign for each force pair can be chosen. Thus, when $\mathbf{r}_c$ exists inside or on the edge of $\triangle 123$, Γ takes the minimum value $\Gamma_{\text{CFD}} = \Gamma_{\text{FCD}}$. Figure 5 shows the minimum value of Γ for each force-center position $\mathbf{r}_c$ for an area potential. Here, HD into three FCD force pairs and two CFD force pairs is used ($f_{12}^{\text{CF}} = 0$, $f_{13}^{\text{CF}} = 0$, or $f_{23}^{\text{CF}} = 0$), since infinitely small values can be taken for all FCD pairs if all six force pairs are allowed. For $\mathbf{r}_c$ lying in the interior region of $\triangle 123$, Γ is constant, while Γ is greater for $\mathbf{r}_c$ lying in the exterior region. Therefore, the Γ minimization implies the restriction on the decomposition choices to the interior region but does not give a unique combination.

When the original force center $\mathbf{r}_{c0}$ exists outside the triangle, Γ typically has the lowest value at a single position of $\mathbf{r}_c$. Figure 6 shows a typical example of Γ in the HD of a bending potential on θ_{123} with $f_{13}^{\text{CF}} = 0$. The deepest minimum of Γ appears between $\mathbf{r}_{c0}$ and the triangle $\triangle 123$ and local minima appear in the other exterior regions. We consider the case where $\mathbf{r}_{c0}$ lies in the region B, as shown in Fig. 3. We
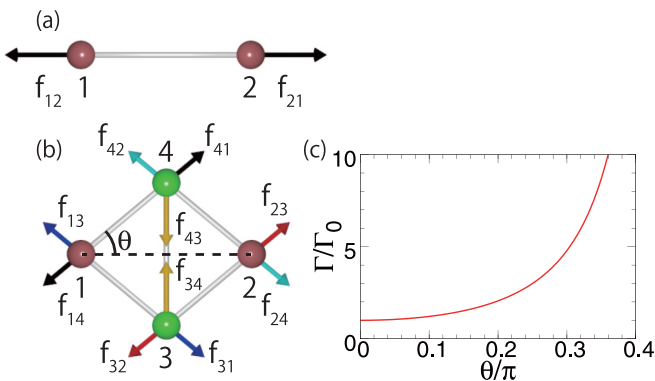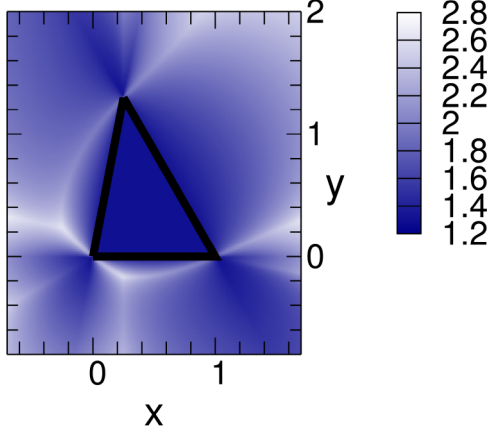
FIG. 5. Contour map of the stress distribution magnitude Γ with respect to the force-center position $\mathbf{r}_c(x, y)$ for the surface tension $k_{ar}A_{123}$. The color bar shows the magnitude of Γ / k_{ar}.

define the position $\mathbf{r}_m$, which is geometrically determined:

$$\mathbf{r}_m = \mathbf{r}_2 + \sqrt{r_{12}r_{23}}\hat{\mathbf{r}}_{bv},$$
$$\hat{\mathbf{r}}_{bv} = \frac{\hat{\mathbf{r}}_{12} + \hat{\mathbf{r}}_{32}}{|\hat{\mathbf{r}}_{12} + \hat{\mathbf{r}}_{32}|}, \tag{18}$$

where $\hat{\mathbf{r}}_{bv}$ is a unit vector bisecting the angle θ_{123}. The triangles $\triangle 12m$ and $\triangle m23$ are similar. When $\mathbf{r}_m$ is in the interior or on the edges of the triangle $\triangle 13c0$ formed by $\mathbf{r}_1$, $\mathbf{r}_3$, and $\mathbf{r}_{c0}$, Γ has the global minimum at $\mathbf{r}_c = \mathbf{r}_m$, where HD is taken for five force pairs, f_{12}^{CF}, f_{23}^{CF}, f_{1m}, f_{2m}, and f_{3m}. This minimum appears not only for the bending forces but also for the other three-body forces with $\mathbf{r}_{c0}$ lying in the region B. The local minimum in the region E with $f_{13}^{CF} = 0$ appears at $\mathbf{r}_{lm} = \mathbf{r}_2 - \sqrt{r_{12}r_{23}}\hat{\mathbf{r}}_{bv}$. The derivations of these global and local minima are described in Appendix C. The stress cross norms are balanced at $\mathbf{r}_m$: $|f_{1m}|r_{1m} = |f_{2m}|r_{2m} = |f_{3m}|r_{3m}$. For the bending forces, the condition for $\mathbf{r}_m$ lying in $\triangle 13c0$ is $r_{12}/r_{23} \geqslant \cos^2(\theta_{123}/2)$ and $r_{23}/r_{12} \geqslant \cos^2(\theta_{123}/2)$. This condition is satisfied in typical simulation conditions, including our present simulation. It is violated only when r_{12}/r_{23} significantly deviates from unity and θ_{123} is small.
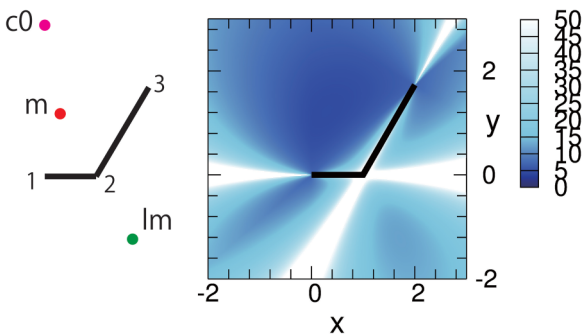

FIG. 6. Contour map of the stress distribution magnitude Γ with respect to the force-center position $\mathbf{r}_c(x, y)$ for the bending potential in Eq. (19). The color bar shows Γ / k_b. The positions of the original force center $\mathbf{r}_{c0}$ and the force centers $\mathbf{r}_m$ and $\mathbf{r}_{lm}$ of the global and local minima of Γ are shown in the left panel.

For general three-body forces, $\mathbf{r}_m$ can be outside $\triangle 13c0$. In this case, we do not have an analytical solution for the Γ minimum, but it can be calculated numerically. In the next section, we investigate how the stress profile of a bilayer membrane depends on the decomposition.

III. BILAYER MEMBRANE

We simulate a tensionless bilayer membrane with various decompositions of bending forces by using coarse-grained and atomistic lipid models. In Sec. III A, the stress profile and Gaussian curvature modulus are discussed by using the dissipative particle dynamics (DPD) method [33–36]. DPD is one of the widely used coarse-grained lipid models. In Sec. III B, the stress profile of an atomistic MD of DOPC (1,2-Dioleoyl-sn-glycero-3-phosphocholine) using the CHARMM36 force field [37,38] is discussed.

We refer to HD with the global and local minima of Γ in the regions B and E as HD (GM) and HD (LM), respectively. In HD, we examine only the case $f_{13}^{CF} = 0$, since HD (GM) and HD (LM) are obtained in this condition.

A. Coarse-grained model

1. Model description

An amphiphilic molecule is represented by a linear chain of four particles: one hydrophilic (H) and three hydrophobic (T) DPD particles. Neighboring DPD particles are connected via the harmonic bond potential, $U_{bond}(r_{ij}) = (k_s/2)(1 - r_{ij}/\ell_0)^2$, with $k_s = 150k_BT$, where k_BT is the thermal energy. One of the simplest bending potentials is employed at the second and third particles of the amphiphile:

$$U_{bend1}(\theta_{ijk}) = k_b(1 - \cos\theta_{ijk}), \tag{19}$$

with $k_b = 30k_BT$. A dihedral potential is not considered. Water is represented by DPD particles labeled W. All particle pairs interact through a soft repulsive potential: $U_{rep}(r_{ij}) = (a_{ij}/2)(1 - r_{ij}/r_{cut})^2$, which vanishes beyond the cutoff at $r_{ij} = r_{cut}$. We set $r_{cut} = 2\ell_0$ in this study. The repulsive interaction parameters a_{ij} are listed in Table I.

The amphiphilic molecules form a bilayer membrane with the bending rigidity $\kappa/k_BT = 18.3 \pm 0.2$, which is a typical value for a bilayer membrane at room temperature [39]. The details of the simulation method are described in Appendix D 1.

2. Lateral pressure profile

The lateral and normal pressure profiles along the normal (z) direction of the bilayer membrane for different force decomposition methods are shown in Fig. 7. The pressure profiles are calculated from the average stress for small slices

TABLE I. Repulsive interaction parameters a_{ij} with unit k_BT.

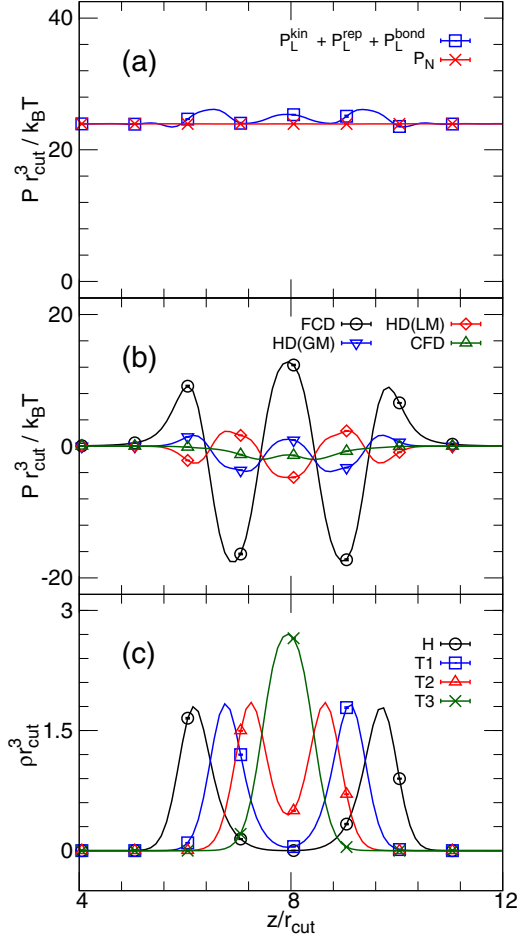|	W	H	T
W	25	25	200
H	25	25	200
T	200	200	25

FIG. 7. Pressure and density profiles along bilayer normal (z) axis obtained by the DPD simulation. (a) Total normal pressure profile $P_N(z)$ and partial lateral pressure profile $P_L(z)$ given by the sum of three contributions of the kinetic, repulsive, and bond potential components. (b) Lateral pressure profile $P_L^{bend1}(z)$ given by bending potential stress with four decomposition methods. (c) Number density profile of four particles in the amphiphilic molecules. H represents the first (hydrophilic head) particle. T1, T2, and T3 represent three hydrophobic particles. The symbols and error bars are shown at several data points.

along the xy plane with a width of $\Delta z = 0.2\ell_0$: $P_L(z) = -[\sigma_{xx}(z) + \sigma_{yy}(z)]/2$ and $P_N(z) = -\sigma_{zz}(z)$. The lateral profile $P_L(z)$ strongly depends on the force decomposition methods, while the normal profile $P_N(z)$ is independent of the decompositions and takes a constant value. The contribution of two-body forces to $P_L(z)$ is only slightly dependent on z [see Fig. 7(a)].

The contribution P_L^{bend1} of the bending forces to the lateral profile is significantly different for different decomposition methods. The amplitude of P_L^{bend1} of FCD is much larger than those of CFD, HD (GM), and HD (LM), as shown in Fig. 7(b). Surprisingly, the function shape of P_L calculated by HD (LM) has the opposite sign those calculated by the other force-decomposition methods. In addition, the pressure peaks of FCD slightly shift to the outside of the position of the head particles of the bilayer [compare Figs. 7(b) and 7(c)]. As mentioned in the previous section, for all force decompositions
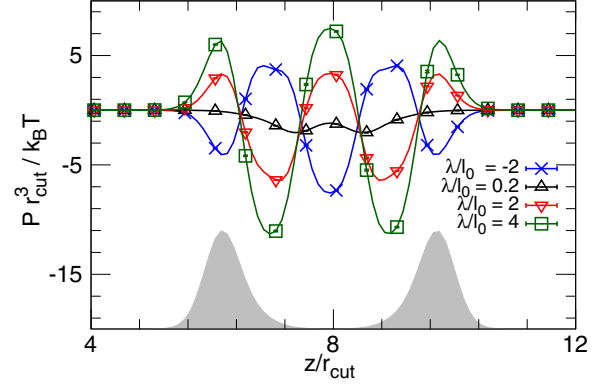

FIG. 8. Length λ dependence of the bending potential contribution P_L^{bend1} to the lateral pressure profile. The symbols and error bars are shown at several data points. The density profile of hydrophilic heads [the same data in Fig. 7(c)] is shown as the gray-filled curve in arbitrary units.

shown in Fig. 7, linear- and angular-momentum conservation are satisfied.

To further examine the dependence of lateral pressure on the force decomposition, we systematically change the force center $\mathbf{r}_c$:

$$\mathbf{r}_c = \mathbf{r}_2 + \lambda \hat{\mathbf{r}}_{bv}, \qquad (20)$$

where λ is the distance between $\mathbf{r}_c$ and $\mathbf{r}_2$. For HD (GM) and HD (LM), $\lambda = \sqrt{r_{12}r_{23}}$ and $\lambda = -\sqrt{r_{12}r_{23}}$, respectively. At $\lambda = 2r_{12}r_{23}\cos(\theta_{123}/2)/(r_{12} + r_{23})$, the decomposition corresponds to CFD, since the force center is on the line segment between $\mathbf{r}_1$ and $\mathbf{r}_3$. Figures 8 and 9 show the dependence of P_L^{bend1} on λ. As λ increases, the lateral pressure increases. A linear relation between λ and P_L^{bend1} (also λ and P_L) is found even for negative values of λ.

This linear dependence on λ is analytically derived when $\hat{\mathbf{r}}_{bv}$ is along the x axis and $\hat{\mathbf{r}}_{12} - \hat{\mathbf{r}}_{32}$ is along the z axis. Since the force pair $\mathbf{f}_{2c}$ contributes to the stress $\sigma_{xx}(z)$ as $f_{2c}\lambda\delta(z - z_2)/A_{xy}$, the lateral stress produced by the bending potential on
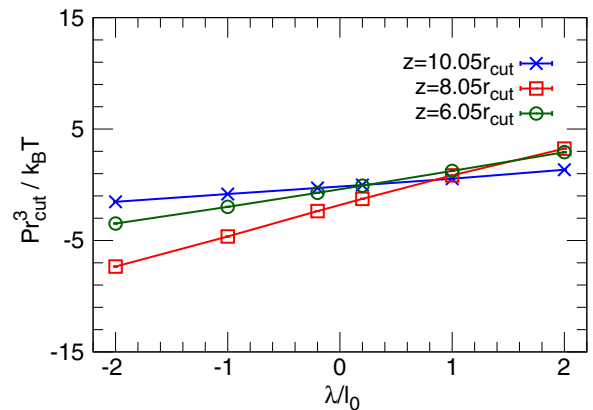

FIG. 9. Contribution of bending potential P_L^{bend1} to the lateral pressure at three xy planes with $z/r_{cut} = 6.05$, 8.05, and 10.05 as a function of λ.

θ_{123} is given by

$$\sigma_{xx}^{\text{bend}}(z) = \frac{f_1 r_{12}}{A_{xy} \sin \varphi} [s_{b1} B(z_1, z_2, z)$$
$$+ s_{b2}\delta(z - z_2) + s_{b3} B(z_3, z_2, z)],$$
$$s_{b1} = -\frac{\lambda}{r_{12}} + 2\cos\varphi - \cos^3\varphi,$$
$$s_{b2} = \frac{r_{12} + r_{23}}{r_{12}r_{23}}\lambda - 2\cos\varphi,$$
$$s_{b3} = -\frac{\lambda}{r_{23}} + 2\cos\varphi - \cos^3\varphi, \tag{21}$$

where $\varphi = \theta_{123}/2$ and A_{xy} is the area of the xy plane. Equation (21) clearly shows that $\sigma_{xx}^{\text{bend}}(z)$ is a linear function of λ for $z_1 < z < z_3$. Our simulation results indicate that this linear relation is approximately satisfied even when averaging the conformations in which $\hat{\mathbf{r}}_{\text{bv}}$ are fluctuated around the xy plane.

3. Gaussian curvature modulus

The Gaussian curvature modulus $\bar{\kappa}$ can be calculated [24–26] as

$$\bar{\kappa} = \int [P_N(z) - P_L(z)]z^2 dz. \tag{22}$$

From elastic theory, $\bar{\kappa}$ is related with κ via [40]

$$\bar{\kappa} = (\nu - 1)\kappa, \tag{23}$$

where ν is the Poisson's ratio of the bilayer membrane. Although Poisson's ratio is generally varied in the range of $-1 \leqslant \nu \leqslant 1/2$, $\bar{\kappa}/\kappa \simeq -1$ was reported in the simulations by Hu *et al.* [24,27] and experiments [41,42]. Hu *et al.* calculated $\bar{\kappa}$ from the shape transition between a disk-shaped bilayer patch and vesicle. They also calculated $\bar{\kappa}$ using the pressure profile with Eq. (22) but concluded that the pressure profile yields unphysical results since the resultant $\bar{\kappa}$ is positive or has a small amplitude compared to κ. However, their pressure-profile calculation was performed by using GLD; hence, the pressure tensor does not satisfy angular-momentum conservation. Recently, Torres-Sánchez *et al.* calculated $\bar{\kappa}$ using CFD [13]. They reported that the calculated $\bar{\kappa}$ agrees well with experimental values.

As described in Sec. III A 2, the lateral pressure profile is strongly dependent on the force-decomposition method. Thus, $\bar{\kappa}$ estimated with Eq. (22) also varies significantly upon changing the force center in HD. Table II lists $\bar{\kappa}$ and $\bar{\kappa}/\kappa$ for four different decomposition methods. CFD, HD (GM), and HD (LM) give $-\bar{\kappa}/\kappa \ll 1$, and FCD gives $-\bar{\kappa}/\kappa > 1$. None of them satisfy $\bar{\kappa}/\kappa \simeq -1$. To further clarify the dependence

TABLE II. Gaussian curvature modulus $\bar{\kappa}$ and its ratio to bending rigidity $\bar{\kappa}/\kappa$ for different force-decomposition methods.

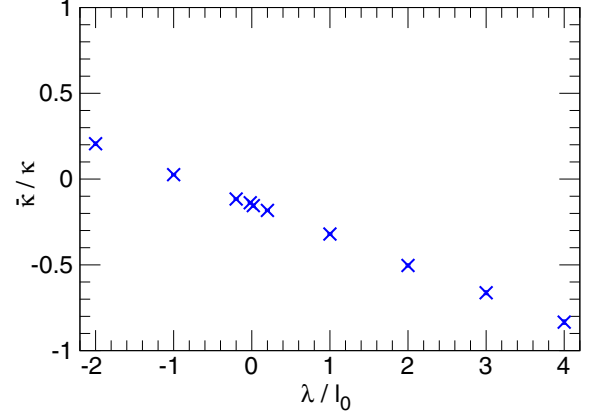|	$\bar{\kappa}/k_B T$	$\bar{\kappa}/\kappa$
CFD	-3.1 ± 0.2	-0.17 ± 0.01
HD (GM)	-6.15 ± 0.09	-0.335 ± 0.006
HD (LM)	0.72 ± 0.07	0.039 ± 0.004
FCD	-32.8 ± 0.1	-1.79 ± 0.02

FIG. 10. Ratio of Gaussian curvature modulus $\bar{\kappa}$ to bending rigidity κ as a function of λ.

of $\bar{\kappa}$ on $\mathbf{r}_c$, we calculated $\bar{\kappa}/\kappa$ as a function of λ. Figure 10 shows the linear dependence of $\bar{\kappa}/\kappa$ on λ. This linearity is the consequence of the linearity of the pressure profile on λ. When $\lambda \simeq 4\ell_0$, $\bar{\kappa}/\kappa \simeq -1$ is obtained. However, this position is too far from the positions of the interacting particles. Thus, it does not seem to be physically plausible. Our results support Hu's conclusion that Eq. (22) gives an unphysical value of $\bar{\kappa}$ in bilayer membranes.

B. Atomistic model

1. Model description

The DOPC molecules are modeled by the recent version of CHARMM all-atom force field (CHARMM36) [37,38], and water molecules are modeled by rigid TIP3P. We apply CFD, FCD, HD (LM), and HD (GM) to the bending potential. The four-body potential contribution to local stress field is calculated by using CFD. The details of the simulation method are described in Appendix D 2.

2. Lateral pressure profile

The lateral pressure profiles along the bilayer normal direction are shown in Fig. 11 for four different force-decomposition methods. The pressure profiles are calculated for small slices with slice width $\Delta z = 0.1$ nm in the same manner as in Sec. III A. The dependence of lateral pressure profile on the force decompositions is qualitatively similar to that of the DPD model but its amplitude becomes much smaller [see Fig. 11(b)]. The differences of force decompositions affect the local pressure at the surface between water and amphiphilic molecules. In the hydrophobic region, there are no significant differences of stress profiles for different force decompositions. Thus, in the higher-resolution model, the decomposition methods of the bending forces modify the pressure profile less than the lower-resolution (coarse-grained) model.

IV. DISCUSSION

The total stress of each three-body potential is independent of the decomposition method. However, the distribution of this stress in 2D space significantly varies even under the strong law
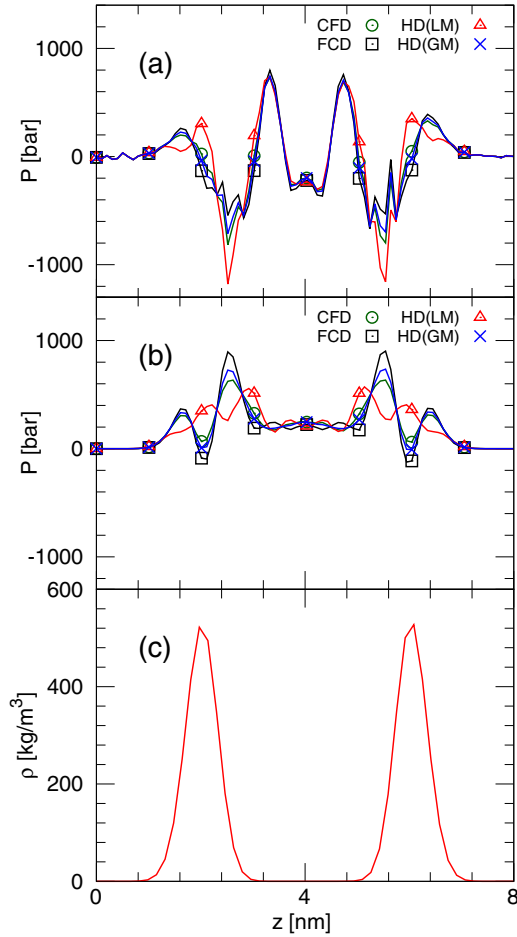
FIG. 11. Pressure and density profiles of DOPC membrane along the bilayer normal (z) axis. (a) Total lateral pressure profile for four force decomposition methods. (b) Partial lateral pressure profile given by the bending potential. (c) Mass density profile of hydrophilic head groups (phosphoric acid and choline groups).

of action and reaction. We introduced the stress distribution magnitude Γ to evaluate the decomposition method. For the area potentials, Γ has the minimum value in the entire triangular region formed by the three particles, whereas Γ has the minimum value at a single position for the bending potentials. Hence, Γ can be used to reduce the candidates for suitable decompositions but the best (unique) decomposition is not determined by Γ, at least for the area potential.

The discrete stress of a molecular simulation can be mapped into the stress field in the continuum space. If the corresponding stress field in the continuum space is known, one can state that the decomposition producing the closest stress is the best choice. In typical simulation conditions, the resultant stress cannot be obtained a priori. However, if a particle potential is constructed as a discretized version of the potential in the continuum space, the corresponding stress field in the continuum space is obtained from the original continuum potential. The surface tension $k_{ar}A_{123}$ is one of the discretized potentials. When a continuum surface with area A is discretized to acute triangles, the surface tension of $k_{ar}A$ is discretized to $k_{ar}\sum_{k}A_{k}$, where A_{k} is the area of the kth triangle. When the triangle is on the xy plane, $\sigma_{xx}(\mathbf{x}) =$

$\sigma_{yy}(\mathbf{x}) = k_{ar}/L_z$ and $\sigma_{xy}(\mathbf{x}) = 0$ are given in the continuum description, where L_z is the side length of the simulation box in the z direction. Both CFD and FCD distribute the stress into line segments so that they deviate from the constant stress field. If HD with multiple force centers distributed on the triangle is employed, a nearly constant stress field can be constructed. Alternatively, Hardy's spatial average with a weighting function [3] also helps CFD and FCD to approach the constant field.

For surface tension or other discretized potentials, the resultant stress field becomes closer to the original continuum field as the surface is discretized into smaller triangles. Thus, it is related with the resolution of the simulation. For classical molecular simulations, local interactions in a length scale smaller than the diameter of atoms or particles are not typically taken into account for coarse graining. For all-atom simulations, the force fields between atoms are constructed from *ab initio* quantum-mechanical calculations [43–45]. Even from the viewpoint of classical mechanics, each particle has a finite size. For a pairwise interaction such as chemical bonds, the stress is distributed not only in the line segment between two particle centers but also in a cylindrical region with the diameter equal to the particle size. Thus, one may have to determine the decomposition method for multibody forces through comparison with the underlying high-resolution potential interactions. For lipid membranes, the pressure profile of the higher-resolution atomistic model has much smaller dependence on the decomposition than that of the lower-resolution (four-particle) DPD model. This also supports our hypothesis on the resolution.

Let us go back to the discussion on the stress field of the bending forces on θ_{123}. CFD and HD (GM) of the bending forces give the stress distribution on the edge of $\mathbf{r}_{13}$ or close to the edge, respectively. If these positions are within the interaction radius of the atom (or particle) at $\mathbf{r}_1$ or $\mathbf{r}_3$, they can be employed as a force-acting point. However, FCD and HD (LM) are unphysical since their force centers are far from the triangle $\triangle 123$ in most of the case. For real bending potentials, the stress distribution may strongly depend on the molecules, but it is likely approximated to the interaction between two chemical bonds (the middle points of $\mathbf{r}_{12}$ and $\mathbf{r}_{23}$). Thus, HD with the force center $\mathbf{r}_c$ lying in the middle of $\triangle 123$ may be a physically reasonable decomposition, where Γ is greater than those of HD (GM) and CFD but the stress profile of the bilayer membranes is flatter.

A coarse-grained model often does not have a specific underlying higher-resolution model. In such a case, one may have to calculate the stress field without the higher-resolution information. We describe our speculative consideration on the choice of the decomposition when the force center $\mathbf{r}_{c0}$ lies in the interior region of the triangle of three interacting particles like in the area potential. In this case, FCD, CFD, and HD which force center lying in the interior of the triangle has the minimum value of Γ. Among of them, FCD gives the minimum of the total length ℓ_{sum}, i.e., the minimum propagation path of the stress. Therefore, the minimum total length may be employed as an additional criterion so that FCD can be chosen.

For n-body forces with $n \geqslant 4$, all of the extrapolations of the force vectors $\mathbf{f}_i$ from $\mathbf{r}_i$ do not typically meet at a single position. Thus, FCD is not generally available for $n \geqslant 4$.

However, FCD can be performed for specific potentials for which all $\mathbf{f}_i$ meet a single position. Let us consider potentials $U_{\mathrm{rg}}(r_{\mathrm{gw}}^2)$ on a weighted radius of gyration $r_{\mathrm{gw}}^2 = \sum_i^n w_i(\mathbf{r}_i - \mathbf{r}_{\mathrm{Gw}})^2$ for a center position $\mathbf{r}_{\mathrm{Gw}} = \sum_i^n w_i\mathbf{r}_i$, where the weight w_i is normalized as $\sum_i^n w_i = 1$. Since all of $\mathbf{f}_i$ meet at $\mathbf{r}_{\mathrm{Gw}}$, these forces are decomposed by FCD with the force center $\mathbf{r}_c = \mathbf{r}_{\mathrm{Gw}}$. If the force center $\mathbf{r}_c = \mathbf{r}_{\mathrm{Gw}}$ or a force center for three of the forces is used, HD is applicable for any n-body force. The center position $\mathbf{r}_c$ can be arbitrarily set by adjusting w_i in $\mathbf{r}_{\mathrm{Gw}}$. Multiple center positions may be useful. However, it has many choices of the force decomposition for $n \geqslant 4$, and it is currently unclear how the force decomposition can be tuned.

V. SUMMARY

We have proposed a decomposition method (FCD) of three-body forces using the position, where three-force extrapolations from the particle positions meet, and combined it with CFD, which decomposes the forces into force pairs between interacting particles. Our study has revealed that the local stress field of three-body forces is strongly dependent on these decomposition methods. We have discussed the choice of the decomposition using the stress distribution magnitude Γ and comparison with the stress fields in continuum fields and in higher resolutions of discretization. We have not reached a concrete conclusion for the best decomposition but rather considered that it depends on the underlying higher-resolution potential.

APPENDIX A: AREA POTENTIAL

Here, we describe the force decomposition of the general form of area potentials, $U_{\mathrm{ar}}(A_{123})$, for the triangle $\triangle 123$. The area is given by $A_{123} = |\mathbf{r}_{12} \times \mathbf{r}_{13}|/2$. The force $\mathbf{f}_1$ is given as

$$\mathbf{f}_1 = -\frac{\partial U_{\mathrm{ar}}}{\partial \mathbf{r}_1} = -\frac{U_{\mathrm{ar}}'}{4A_{123}}[r_{23}^2\mathbf{r}_{13} - (\mathbf{r}_{13} \cdot \mathbf{r}_{23})\mathbf{r}_{23}], \quad (A1)$$

where $U_{\mathrm{ar}}' = \partial U_{\mathrm{ar}}/\partial A_{123}$. This force $\mathbf{f}_1$ is perpendicular to $\mathbf{r}_{23}$, since the area does not change if $\mathbf{r}_1$ moves parallel to $\mathbf{r}_{23}$. For the potential of the surface tension $U_{\mathrm{ar}}(A_{123}) = k_{\mathrm{ar}}A_{123}$, $U_{\mathrm{ar}}' = k_{\mathrm{ar}}$.

The force f_{12} in CFD is obtained by the decomposition of $\mathbf{f}_1$ into components along $\hat{\mathbf{r}}_{12}$ and $\hat{\mathbf{r}}_{13}$ or directly by using $f_{12} = -\partial U_{\mathrm{ar}}/\partial r_{12}|r_{13}, r_{23}$ with Heron's formula $A_{123} = \sqrt{b(b - r_{12})(b - r_{13})(b - r_{23})}$, where $b = (r_{12} + r_{13} + r_{23})/2$:

$$f_{12} = -\frac{U_{\mathrm{ar}}'}{4A_{123}}(\mathbf{r}_{13} \cdot \mathbf{r}_{23})r_{12}. \quad (A2)$$

The other forces $\mathbf{f}_2$, $\mathbf{f}_3$, f_{13}, and f_{23} are similarly obtained. The original force center $\mathbf{r}_{c0}$ is the orthocenter of $\triangle 123$. Since $q = 1/4U_{\mathrm{ar}}'^2 > 0$, $\mathbf{r}_{c0}$ lies in the interior region or exterior region A, C, or E of $\triangle 123$ depicted in Fig. 3. When $\triangle 123$ is an

acute triangle, $\mathbf{r}_{c0}$ lies in the interior region. When the angle θ_{123} is obtuse ($\mathbf{r}_{12} \cdot \mathbf{r}_{32} < 0$), $\mathbf{r}_{c0}$ lies in the exterior region E.

APPENDIX B: BENDING POTENTIAL

Next, we describe the force decomposition of the general form of bending potentials, $U_{\mathrm{bend}}(\hat{\mathbf{r}}_{12} \cdot \hat{\mathbf{r}}_{32})$, for the angle $\theta_{123} = \cos^{-1}(\hat{\mathbf{r}}_{12} \cdot \hat{\mathbf{r}}_{32})$ of three particle positions $\mathbf{r}_1$, $\mathbf{r}_2$, and $\mathbf{r}_3$. The forces on the three particles are given by

$$\mathbf{f}_1 = -\frac{U_{\mathrm{bend}}'}{r_{12}}[\hat{\mathbf{r}}_{32} - (\hat{\mathbf{r}}_{12} \cdot \hat{\mathbf{r}}_{32})\hat{\mathbf{r}}_{12}],$$

$$\mathbf{f}_2 = -\frac{U_{\mathrm{bend}}'}{r_{12}r_{32}}\left[\frac{(\mathbf{r}_{12} \cdot \mathbf{r}_{32} - r_{12}^2)\hat{\mathbf{r}}_{12}}{r_{12}} + \frac{(\mathbf{r}_{12} \cdot \mathbf{r}_{32} - r_{32}^2)\hat{\mathbf{r}}_{32}}{r_{32}}\right],$$

$$\mathbf{f}_3 = -\frac{U_{\mathrm{bend}}'}{r_{32}}[\hat{\mathbf{r}}_{12} - (\hat{\mathbf{r}}_{12} \cdot \hat{\mathbf{r}}_{32})\hat{\mathbf{r}}_{32}]. \quad (B1)$$

The forces $\mathbf{f}_1$ and $\mathbf{f}_3$ are perpendicular to $\mathbf{r}_{12}$ and $\mathbf{r}_{32}$, respectively, since θ_{123} is independent of the lengths r_{12} and r_{32}. For the bending potential of Eq. (19), $U_{\mathrm{bend}}' = -k_{\mathrm{b}}$.

In CFD, these forces are decomposed into the following force pairs:

$$f_{12} = -U_{\mathrm{bend}}'\frac{\mathbf{r}_{12} \cdot \mathbf{r}_{13}}{r_{12}^2r_{23}},$$

$$f_{13} = U_{\mathrm{bend}}'\frac{r_{13}}{r_{12}r_{23}}, \quad (B2)$$

$$f_{23} = -U_{\mathrm{bend}}'\frac{\mathbf{r}_{23} \cdot \mathbf{r}_{13}}{r_{12}r_{23}^2}.$$

These force pairs can be obtained from Eqs. (B1) and (12) or directly from $f_{12} = -\partial U_{\mathrm{bend}}/\partial r_{12}|r_{13}, r_{23}$ with $\hat{\mathbf{r}}_{12} \cdot \hat{\mathbf{r}}_{32} = (r_{12}^2 + r_{23}^2 - r_{13}^2)/2r_{12}r_{23}$. The original force center $\mathbf{r}_{c0}$ always lies in the exterior region of $\triangle 123$, since $q = -4A_{123}^2/r_{12}^4r_{23}^4U_{\mathrm{bend}}'^2 < 0$. When the angles $\theta_{312} < \pi/2$ and $\theta_{231} < \pi/2$, $f_{12}f_{23} > 0$ and $f_{12}f_{13} < 0$ so that $\mathbf{r}_{c0}$ lies in the exterior region B depicted in Fig. 3. For $\theta_{312} > \pi/2$ or $\theta_{231} > \pi/2$, $\mathbf{r}_{c0}$ lies in the region D or F, respectively. The stress distribution magnitudes Γ for FCD and CFD take the same value for the bending potentials: $\Gamma_{\mathrm{FCD}} = \Gamma_{\mathrm{CFD}} = 2r_{13}^2|U_{\mathrm{bend}}'|/r_{12}r_{23}$ for $\theta_{312} < \pi/2$ and $\theta_{231} < \pi/2$, and $\Gamma_{\mathrm{FCD}} = \Gamma_{\mathrm{CFD}} = 2\mathbf{r}_{12} \cdot \mathbf{r}_{13}|U_{\mathrm{bend}}'|/r_{12}r_{23}$ for $\theta_{231} > \pi/2$. For the typical simulation conditions including our present simulation, θ_{312} and θ_{231} are small. Thus, we consider only the case of $\mathbf{r}_{c0}$ lying in region B in this paper.

APPENDIX C: MINIMIZATION OF STRESS DISTRIBUTION MAGNITUDE FOR EXTERIOR FORCE CENTER

Here, we consider the force center $\mathbf{r}_c$ for the minimum of the stress distribution magnitude Γ, when $\mathbf{r}_{c0}$ lies in the exterior region B, where $f_{12}f_{13} < 0$, $f_{12}f_{23} > 0$, and $q < 0$. As mentioned in Sec. II C, Γ takes the lowest value at the position $\mathbf{r}_{\mathrm{m}}$ given in Eq. (18) for HD with $f_{13}^{\mathrm{CFD}} = 0$, if $\mathbf{r}_{\mathrm{m}}$ is in the interior region surrounded by three positions $\mathbf{r}_1$, $\mathbf{r}_3$, and $\mathbf{r}_{c0}$. This position is derived as follows: We consider the minimization of the difference

$\Gamma_{\text{dif}} = \Gamma - \Gamma_{\text{CFD}} = \Gamma_{\text{HD}}^{\text{FC}} - (|f_{12}^{\text{FC}}|r_{12} + |f_{13}^{\text{FC}}|r_{13} + |f_{23}^{\text{FC}}|r_{23})$, since the contribution of the CFD force pairs does not explicitly appear in Γ_{dif}:

$$\Gamma_{\text{dif}} = \frac{2\tilde{f}_{12}^{\text{FC}}\tilde{f}_{23}^{\text{FC}}}{|q|}(|\tilde{f}_{12}^{\text{FC}}|r_{12}^2 + |\tilde{f}_{23}^{\text{FC}}|r_{23}^2 - |\tilde{f}_{13}^{\text{FC}}|r_{13}^2)$$

$$= 2|\tilde{f}_{13}^{\text{FC}}|r_{13}^2 g(x,y), \tag{C1}$$

where

$$g(x,y) = \frac{xy[(\frac{r_{12}}{r_{13}})^2 x + (\frac{r_{23}}{r_{13}})^2 y - 1]}{x + y - xy}, \tag{C2}$$

$$x = -\frac{\tilde{f}_{12}^{\text{FC}}}{\tilde{f}_{13}^{\text{FC}}} \quad \text{and} \quad y = -\frac{\tilde{f}_{23}^{\text{FC}}}{\tilde{f}_{13}^{\text{FC}}}. \tag{C3}$$

The force ratios x and y for the minimum of g are obtained from $\partial g/\partial x = 0$ and $\partial g/\partial y = 0$ as

$$g(x_{\text{GM}}, y_{\text{GM}}) = -\frac{r_{12} + r_{23} - \sqrt{(r_{12} + r_{23})^2 - r_{13}^2}}{r_{12} + r_{23} + \sqrt{(r_{12} + r_{23})^2 - r_{13}^2}} < 0, \tag{C4}$$

with

$$x_{\text{GM}} = \frac{r_{12} + r_{23} - \sqrt{(r_{12} + r_{23})^2 - r_{13}^2}}{r_{12}}, \tag{C5}$$

$$y_{\text{GM}} = \frac{r_{12} + r_{23} - \sqrt{(r_{12} + r_{23})^2 - r_{13}^2}}{r_{23}}. \tag{C6}$$

The position $\mathbf{r}_m$ in Eq. (18) is given by x_{GM} and y_{GM}. To minimize Γ_{dif}, the factor $|f_{13}^{\text{FC}}|$ in Eq. (C1) is taken as the maximum value while maintaining $|f_{13}^{\text{FC}}| + |f_{13}^{\text{CF}}| = |f_{13}^{\text{all}}|$, i.e., $f_{13}^{\text{CF}} = 0$. Hence, the lowest value of Γ is obtained for HD with the force center of $\mathbf{r}_m$ and $f_{13}^{\text{CF}} = 0$.

The local minimum in the region E (LM) is derived from the minimization of $\Gamma + \Gamma_{\text{CFD}} = -2|\tilde{f}_{13}^{\text{FC}}|r_{13}^2 g(x,y)$, since $f_{12}^{\text{CF}} f_{12}^{\text{FC}} < 0$, $f_{23}^{\text{CF}} f_{23}^{\text{FC}} < 0$, and $f_{13}^{\text{CF}} = 0$. The maximum of g is given at

$$x_{\text{LM}} = \frac{r_{12} + r_{23} + \sqrt{(r_{12} + r_{23})^2 - r_{13}^2}}{r_{12}}, \tag{C7}$$

$$y_{\text{LM}} = \frac{r_{12} + r_{23} + \sqrt{(r_{12} + r_{23})^2 - r_{13}^2}}{r_{23}}. \tag{C8}$$

Hence, the local-minimum position is determined as $\mathbf{r}_{\text{lm}} = \mathbf{r}_2 - \sqrt{r_{12}r_{23}}\hat{\mathbf{r}}_{\text{bv}}$ from x_{LM} and y_{LM}.

APPENDIX D: SIMULATION METHOD

1. Coarse-grained model

In the DPD method, the particle motions are integrated in the following Newton's equation with the DPD thermostat:

$$m\frac{d\mathbf{v}_i}{dt} = -\frac{\partial U}{\partial \mathbf{r}_i} + \sum_{j \neq i}[-w(r_{ij})\mathbf{v}_{ij} \cdot \hat{\mathbf{r}}_{ij} + \sqrt{w(r_{ij})}\xi_{ij}(t)]\hat{\mathbf{r}}_{ij},$$
$$\tag{D1}$$

where $U = \sum_{i>j} U_{\text{rep}}(r_{ij}) + \sum_{\text{bonds}} U_{\text{bond}}(r_{ij}) + \sum_{\text{angles}} U_{\text{bend1}}(\theta_{ijk})$ and $w(r_{ij}) = \gamma(1 - r_{ij}/r_{\text{cut}})$, with the cutoff at $r_{ij} = r_{\text{cut}}$ where $\gamma = 4.5\sqrt{k_B T m}/r_{\text{cut}}$. The Gaussian white noise $\xi_{ij}(t)$ satisfies the fluctuation-dissipation theorem, i.e., $\langle \xi_{ij}(t) \rangle = 0$ and $\langle \xi_{ij}(t)\xi_{i'j'}(t') \rangle = 2k_B T(\delta_{ii'}\delta_{jj'} + \delta_{ij'}\delta_{ji'})\delta(t - t')$.

We discretize Eq. (D1) by using Shardlow's S1 splitting algorithm [46]. We employ the multi-time-step algorithm [47,48], the time step of which, $\Delta t = 0.05\tau$, is different from the integration time step $\delta t = 0.005\tau$ for a conservative force $-\partial U/\partial \mathbf{r}_i$, where $\tau = r_{\text{cut}}\sqrt{m/k_B T}$.

All simulations are carried out under the NVT ensemble at the particle density $N/V = 3/r_{\text{cut}}^3$ with a periodic boundary condition. The pressure profiles are calculated for a tensionless membrane at $N_{\text{amp}} = 738$, $N_w = 9336$, and the side lengths of the simulation box $L_x = L_y = L_z = 16r_{\text{cut}}$ by using the IKN procedure with the decomposition described in Sec. II, where N_{amp} and N_w are the numbers of amphiphilic molecules and water particles, respectively. Amphiphilic molecules are preformed into a flat bilayer to reduce the equilibration time. After the equilibration time $\tau_{\text{eq}} = 10\,000\tau$ or $15\,000\tau$, production runs are carried out during 5000τ. The bending rigidity κ of the bilayer membrane is estimated at $N_{\text{amp}} = 2950$ and $N_w = 86\,504$ by using the undulation mode of a nearly planar tensionless membrane [49–51], $\langle |h(q)|^2 \rangle = k_B T/\kappa q^4$, with the extrapolation of the cutoff wavelength, $q_{\text{cut}} \to 0$ [52], where $h(q)$ is the Fourier transformation of bilayer height $h(x,y)$. Error bars are calculated from five independent runs.

2. Atomistic model

MD simulations are carried out in the NPT ensemble using the standard version of GROMACS 5.1 simulation packages [53,54]. Bilayer membranes consisting of 400 DOPC molecules surrounded by 20 000 water molecules are simulated under $T = 303.15\,°\text{C}$ and $P = 1$ bar. The temperature and pressure are controlled by the Nosé–Hoover and Parrinello–Rahman methods, respectively. Newton's equation is integrated by using the leapfrog algorithm with MD time step $\delta t = 2$ fs. A bond constraint is applied to the bonds with hydrogens by using the linear constraint solver (LINCS) algorithm. Long-range electrostatic interactions are calculated via the particle mesh Ewald (PME) method. All initial configurations and input parameters are generated using CHARMM-GUI membrane builder [55,56]. The total simulation time is 600 ns, and the first 360 ns is taken as the equilibration time.

The obtained MD trajectories are fed into a customized version of GROMACS-LS [57] to calculate the local stress profiles. The dihedral contribution to local stress is calculated by using CFD. The electrostatic contribution is calculated by using the IKN procedure with cutoff length $r_{\text{cut}}^{\text{el}} = 2.2$ nm. Venegas et al. examined the electrostatic contributions to the local pressure profile using the IKN procedure with finite cutoff by changing $r_{\text{cut}}^{\text{el}}$ and reported that the local stress profile shows little difference at $r_{\text{cut}}^{\text{el}} > 2.2$ nm [12].

[1] J. Irving and J. G. Kirkwood, J. Chem. Phys. **18**, 817 (1950).

[2] W. Noll, J. Ration. Mech. Anal. **4**, 627 (1955).

[3] R. J. Hardy, J. Chem. Phys. **76**, 622 (1982).

[4] P. Schofield and J. Henderson, Proc. R. Soc. London, Ser. A **379**, 231 (1982).

[5] B. D. Todd, D. J. Evans, and P. J. Daivis, Phys. Rev. E **52**, 1627 (1995).

[6] R. Goetz and R. Lipowsky, J. Chem. Phys. **108**, 7397 (1998).

[7] H. Heinz, W. Paul, and K. Binder, Phys. Rev. E **72**, 066704 (2005).

[8] N. C. Admal and E. B. Tadmor, J. Elasticity **100**, 63 (2010).

[9] N. C. Admal, Ph.D. thesis, The University of Minnesota, 2014, http://conservancy.umn.edu/handle/11299/171066.

[10] N. C. Admal and E. Tadmor, J. Chem. Phys. **134**, 184106 (2011).

[11] N. C. Admal and E. Tadmor, J. Mech. Phys. Solids **93**, 72 (2016).

[12] J. M. Vanegas, A. Torres-Sánchez, and M. Arroyo, J. Chem. Theory Comput. **10**, 691 (2014).

[13] A. Torres-Sánchez, J. M. Vanegas, and M. Arroyo, Phys. Rev. Lett. **114**, 258102 (2015).

[14] A. Torres-Sánchez, J. M. Vanegas, and M. Arroyo, J. Mech. Phys. Solids **93**, 224 (2016).

[15] A. D. MacKerell, M. Feig, and C. L. Brooks, J. Comput. Chem. **25**, 1400 (2004).

[16] H. Noguchi and G. Gompper, Phys. Rev. E **73**, 021903 (2006).

[17] S. Takada, Z. Luthey-Schulten, and P. G. Wolynes, J. Chem. Phys. **110**, 11616 (1999).

[18] H. Noguchi and M. Takasu, Phys. Rev. E **64**, 041913 (2001).

[19] J. N. Israelachvili, *Intermolecular and Surface Forces*, 3rd ed. (Academic Press, Burlington, 2011).

[20] B. Różycki and R. Lipowsky, J. Chem. Phys. **142**, 054101 (2015).

[21] R. M. Venable, F. L. Brown, and R. W. Pastor, Chem. Phys. Lipids **192**, 60 (2015).

[22] M. Orsi, D. Y. Haubertin, W. E. Sanderson, and J. W. Essex, J. Phys. Chem. B **112**, 802 (2008).

[23] M. Orsi and J. W. Essex, PLoS ONE **6**, e28637 (2011).

[24] M. Hu, D. H. de Jong, S. J. Marrink, and M. Deserno, Faraday Discuss. **161**, 365 (2013).

[25] S. Safran, *Statistical Thermodynamics on Surfaces and Interfaces* (Westview Press, Oxford, 2003).

[26] W. Helfrich, J. Phys.: Condens. Matter **6**, A79 (1994).

[27] M. Hu, J. J. Briguglio, and M. Deserno, Biophys. J. **102**, 1403 (2012).

[28] W. Shinoda, T. Nakamura, and S. O. Nielsen, Soft Matter **7**, 9012 (2011).

[29] M. Sotomayor and K. Schulten, Biophys. J. **87**, 3050 (2004).

[30] J. M. Vanegas and M. Arroyo, PLoS ONE **9**, e113947 (2014).

[31] M. D. Fraňová, I. Vattulainen, and O. S. Ollila, Biochim. Biophys. Acta, Biomembr. **1838**, 1406 (2014).

[32] R. H. Templer, S. J. Castle, A. R. Curran, G. Rumbles, and D. R. Klug, Faraday Discuss. **111**, 41 (1999).

[33] R. D. Groot and P. B. Warren, J. Chem. Phys. **107**, 4423 (1997).

[34] M. Venturoli, M. M. Sperotto, M. Kranenburg, and B. Smit, Phys. Rep. **437**, 1 (2006).

[35] P. J. Hoogerbrugge and J. M. V. A. Koelman, Europhys. Lett. **19**, 155 (1992).

[36] P. Espanol and P. Warren, Europhys. Lett. **30**, 191 (1995).

[37] J. B. Klauda, V. Monje, T. Kim, and W. Im, J. Phys. Chem. B **116**, 9424 (2012).

[38] J. B. Klauda, R. M. Venable, J. A. Freites, J. W. O'Connor, D. J. Tobias, C. Mondragon-Ramirez, I. Vorobyov, A. D. MacKerell Jr, and R. W. Pastor, J. Phys. Chem. B **114**, 7830 (2010).

[39] *Structure and Dynamics of Membranes*, edited by R. Lipowsky and E. Sackmann (Elsevier Science, Amsterdam, 1995).

[40] L. D. Landau, E. M. Lifshitz, A. M. Kosevich, and L. P. Pitaevski, *Theory of Elasticity*, 3rd ed. (Elsevier, New York, 1986).

[41] T. Baumgart, S. Das, W. Webb, and J. Jenkins, Biophys. J. **89**, 1067 (2005).

[42] S. Semrau, T. Idema, L. Holtzer, T. Schmidt, and C. Storm, Phys. Rev. Lett. **100**, 088101 (2008).

[43] A. D. Mackerell, J. Comput. Chem. **25**, 1584 (2004).

[44] W. D. Cornell, P. Cieplak, C. I. Bayly, I. R. Gould, K. M. Merz, D. M. Ferguson, D. C. Spellmeyer, T. Fox, J. W. Caldwell, and P. A. Kollman, J. Am. Chem. Soc. **117**, 5179 (1995).

[45] A. D. MacKerell Jr, D. Bashford, M. Bellott, R. L. Dunbrack Jr, J. D. Evanseck, M. J. Field, S. Fischer, J. Gao, H. Guo, S. Ha *et al.*, J. Phys. Chem. B **102**, 3586 (1998).

[46] T. Shardlow, SIAM J. Sci. Comput. **24**, 1267 (2003).

[47] M. Tuckerman, B. J. Berne, and G. J. Martyna, J. Chem. Phys. **97**, 1990 (1992).

[48] H. Noguchi and G. Gompper, Europhys. Lett. **78**, 36002 (2007).

[49] R. Goetz, G. Gompper, and R. Lipowsky, Phys. Rev. Lett. **82**, 221 (1999).

[50] E. Lindahl and O. Edholm, Biophys. J. **79**, 426 (2000).

[51] V. A. Harmandaris and M. Deserno, J. Chem. Phys. **125**, 204905 (2006).

[52] H. Shiba and H. Noguchi, Phys. Rev. E **84**, 031926 (2011).

[53] M. J. Abraham, T. Murtola, R. Schulz, S. Páll, J. C. Smith, B. Hess, and E. Lindahl, SoftwareX **1**, 19 (2015).

[54] S. Pall, M. J. Abraham, C. Kutzner, B. Hess, and E. Lindahl, in *International Conference on Exascale Applications and Software*, edited by S. Markidis and E. Laure (Springer, Stockholm, 2014), pp. 3–27.

[55] S. Jo, T. Kim, V. G. Iyer, and W. Im, J. Comput. Chem. **29**, 1859 (2008).

[56] J. Lee, X. Cheng, J. M. Swails, M. S. Yeom, P. K. Eastman, J. A. Lemkul, S. Wei, J. Buckner, J. C. Jeong, Y. Qi *et al.*, J. Chem. Theory Comput. **12**, 405 (2015).

[57] J. M. Vanegas, A. Torres-Sánchez, and M. Arroyo, *Computing the Local Stress Tensor in Classical MD Simulations*, Polytechnic University of Catalonia, 2016, http://www.lacan.upc.edu/LocalStressFromMD/